www.acsnano.org

Collective Plasmon Coupling in Gold Nanoparticle Clusters for Highly Efficient Photothermal Therapy

Jinxing Chen, Mingfu Gong, Yulong Fan, Ji Feng, Lili Han, Huolin L. Xin, Muhan Cao, Qiao Zhang, Dong Zhang, Dangyuan Lei,* and Yadong Yin*



Downloaded via UNIV OF CALIFORNIA RIVERSIDE on June 30, 2022 at 18:05:04 (UTC). See https://pubs.acs.org/sharingguidelines for options on how to legitimately share published articles.

Cite This: ACS Nano 2022, 16, 910-920



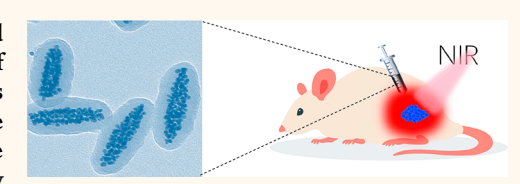
ACCESS

Metrics & More

Article Recommendations

si Supporting Information

ABSTRACT: Plasmonic nanomaterials with strong absorption at near-infrared frequencies are promising photothermal therapy agents (PTAs). The pursuit of high photothermal conversion efficiency has been the central focus of this research field. Here, we report the development of plasmonic nanoparticle clusters (PNCs) as highly efficient PTAs and provide a semiquantitative approach for calculating their resonant frequency and absorption efficiency by combining the effective medium approximation (EMA) theory and full-wave



electrodynamic simulations. Guided by the theoretical prediction, we further develop a universal strategy of space-confined seeded growth to prepare various PNCs. Under optimized growth conditions, we achieve a record photothermal conversion efficiency of up to ~84% for gold-based PNCs, which is attributed to the collective plasmon-coupling-induced near-unity absorption efficiency. We further demonstrate the extraordinary photothermal therapy performance of the optimized PNCs in *in vivo* application. Our work demonstrates the high feasibility and efficacy of PNCs as nanoscale PTAs.

KEYWORDS: plasmon coupling, metal nanostructures, photothermal therapy, confined nanospace, templating seeded growth

ancer is the leading cause of death, with rapidly growing mortality worldwide. Statistics show that the global cancer burden had reached 19.3 million new cases and 10 million deaths in 2020. The International Agency for Research on Cancer (IARC) estimates that one in five people worldwide develops cancer during their lifetime. 1,2 Surgery, chemotherapy, and radiotherapy are currently available clinical approaches for most cancer patients. However, most cancers are diagnosed in the later stage when surgical resection is no longer feasible. Traditional chemotherapy and radiotherapy have poor efficiency due to the unavoidable resistance to drugs and radiation.^{3,4} As an emerging cancer treatment method, photothermal therapy (PTT) has attracted significant attention due to its noninvasive nature, high specificity and efficiency, as well as insignificant side effects. 5-8 For example, when the local temperature increases to above 48 °C, irreversible damage and eventually apoptosis of cancer cells will occur within 4-6 min. Moreover, hyperthermia within cancer cells can induce the release of cancer antigens and proinflammatory cytokines to promote anticancer immunity, which kill the cancer cells synergistically.10

It is known that photothermal therapy agents (PTAs) are essential in PTT. In particular, the PTAs with higher photothermal conversion efficiency (PCE) can convert light energy to heat more effectively, thereby causing less photo-

damage on adjacent healthy tissues. Among the various PTAs, metallic nanostructures with pronounced localized surface plasmon resonance (LSPR) absorption are considered to be promising candidates, mainly due to their high absorption efficiency (absorption efficiency = $\frac{\sigma_{abs}}{\sigma_{abs} + \sigma_{sca}} = \frac{\sigma_{abs}}{\sigma_{ext}}$, where σ_{abs} , σ_{sca} and σ_{ext} represent absorption, scattering, and extinction cross sections of the nanoparticle, respectively). 11 Note that the absorption efficiency of plasmonic PTAs is equivalent to their PCE when all of the absorbed light is converted to heat. Increasing the therapeutic depth requires the absorption peak of plasmonic PTAs to be shifted to the biological transparency window, calling for the delicate design of nanostructures with anisotropic shapes. 12,13 Meanwhile, to ensure a higher absorption efficiency, the anisotropic plasmonic PTAs are required to have a small effective size, which can be seen from the volume dependences of σ_{abs} and σ_{sca} :

Received: September 26, 2021 Accepted: January 7, 2022 Published: January 13, 2022





© 2022 American Chemical Society

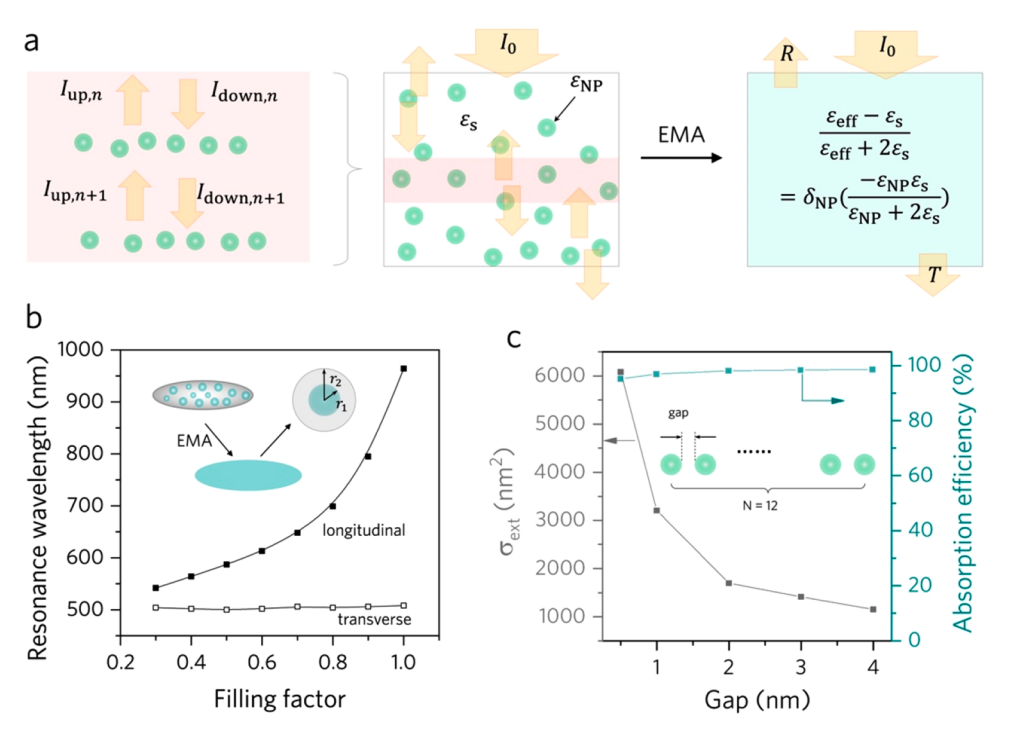


Figure 1. Evaluation of the collective plasmon coupling in PNCs by the EMA theory and full-wave electromagnetic simulations. (a) Schematic illustrations of multilayered (left) and randomly distributed (middle) Au nanospheres in water under light illumination from the topside and the principle of the EMA theory (right). (b) Simulated resonance wavelength of a $130 \times 26 \times 26$ nm³ nanoellipsoid (black squares) versus the FF of Au nanospheres in a PNC. The left inset sketches an actual ellipsoid-shaped PNC, modeled as a homogeneous nanoellipsoid (bottom inset) in the full-wave simulations. The nanoellipsoid has an effective dielectric function defined by the Maxwell–Garnett approximation using the FF of (r_1/r_2) , where r_1 refers to the radius of the spherical inclusion and r_2 refers to the radius of the spherical medium of each unit cell in the PNC (right inset). (c) Maximum extinction cross section and corresponding absorption efficiency versus the gap size of a one-dimensional Au nanoparticle chain. Inset sketches the model chain consisting of 12 Au nanospheres used in the full-wave simulations.

$$\sigma_{abs} = \frac{2\pi}{3\lambda} \varepsilon_{m}^{3/2} V \sum_{i} \frac{\varepsilon_{2}/(n^{(i)})^{2}}{(\varepsilon_{1} + [(1 - n^{(i)})/n^{(i)}]\varepsilon_{m})^{2} + \varepsilon_{2}^{2}}$$
(1)

$$\sigma_{\rm sca} = \frac{8\pi^3}{9\lambda^4} \varepsilon_{\rm m}^2 V^2 \sum_{i} \frac{[(\varepsilon_1 - \varepsilon_{\rm m})^2 + \varepsilon_2^2]/(n^{(i)})^2}{(\varepsilon_1 + [(1 - n^{(i)})/n^{(i)}]\varepsilon_{\rm m})^2 + \varepsilon_2^2}$$
(2)

where λ is the wavelength of light, $\varepsilon_{\rm m}$ the dielectric constant of the surrounding medium, ε the dielectric constant of the metal given by $\varepsilon=\varepsilon_1+i\varepsilon_2$ (ε_1 and ε_2 are the real and imaginary parts of the dielectric constant, respectively), V the volume of the nanoparticle, and $n^{(i)}$ the depolarization factor in the *i*th direction. Typically, when the effective size of a plasmonic nanostructure is reduced to below 20 nm, the absorption efficiency approaches unity in the entire visible spectrum (Figure S1 in the Supporting Information).¹⁴ However, small anisotropic plasmonic PTAs are vulnerable to laser irradiation and tend to undergo shape-morphing during light irradiation, making their PTT efficacy unstable in the treatment. 15,16 The stability of anisotropic plasmonic PTAs can be improved by increasing their sizes, but doing so also increases the light scattering by the materials and negatively affects the PCE. In addition, upon the LSPR excitation in a metallic nanostructure, the absorption and scattering cross sections reach their maximum values simultaneously because they both rely on the plasmon resonance of the nanostructure. As a result, a large amount of light is scattered out of the plasmonic heating system, 17,18 which is not conducive to photothermal

conversion. So far, the experimentally measured PCEs of anisotropic plasmonic PTAs are usually less than 50%, which are much lower than the theoretical value (>90%).¹⁹

Recently, plasmonic nanoparticle clusters (PNCs) have emerged as efficient PTAs.^{20–24} Different from anisotropic plasmonic PTAs, the heat generation in PNCs mainly depends on plasmon resonance coupling. Upon light irradiation, collective plasmon coupling occurs within the cluster, which red shifts the resonance wavelength to the biowindow and also significantly boosts the electromagnetic field intensity in the interparticle gaps by several orders of magnitude.^{25,26} It is worth noting that PNCs are composed of many isotropic nanospheres in small sizes so that the absorption efficiency and light/heat conversion stability can be improved simultaneously.

Although PNCs have promising prospects for PTT, few related studies have been made in this context so far. One reason is probably the lack of theoretical analysis on their optical properties, unlike those widely studied plasmonic oligomers consisting of strongly coupled nanoparticles with the regular arrangement, ^{27,28} whose plasmonic responses can be well-predicted by the well-known plasmon hybridization and Fano theories. ²⁹ To this end, we employ the effective medium approximation (EMA) theory to semiquantitatively determine the optical response of the PNC system, calculate the filling factor-dependent collective resonance wavelength, and discuss the advantage of using densely packed PNCs. Experimentally, we develop a universal strategy of space-confined seeded growth to prepare various PNCs, including plasmonic nanovesicles (Au, Ag) and rod-like plasmonic clusters (Ag,

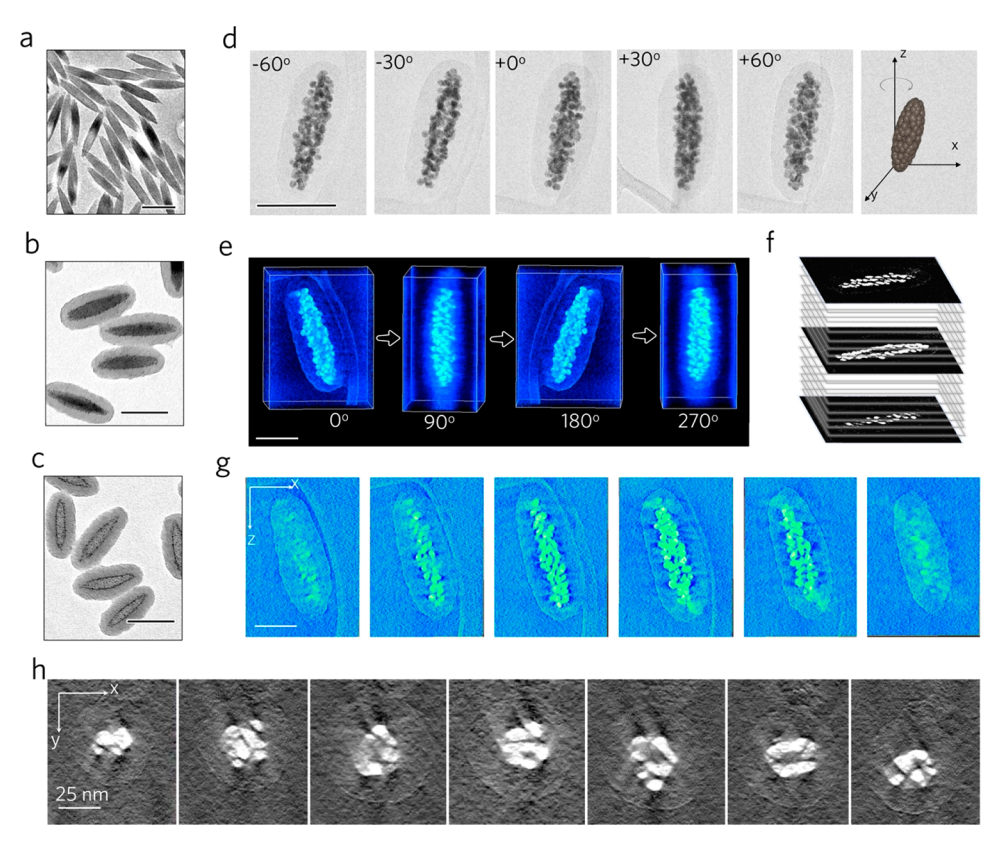


Figure 2. Synthesis and characterization of Au-based PNCs. (a-d) TEM micrographs of FeOOH (a), FeOOH/Au@RF (b), hollow templates containing Au seeds (c), and a Au-based PNC viewed at varied tilt angle (d). (e) Reconstructed 3D images of a Au-based PNC at different rotation angles (0, 90, 180, and 270°). The bright dots represent the Au nanoparticles in the PNC. (f) Schematic illustration of ortho-slices of the reconstructed structure. The x-z plane (g) and x-y plane (h) ortho-slices of the reconstructed structure in (e). Scale bars from (a) to (g) are all 100 nm.

Au, and Cu), and reveal the detailed synthesis mechanism of the Au nanoparticle clusters. We show that optimizing the structure parameters of Au nanoparticle clusters can increase their PCE to 84%, which is much higher than most of the other plasmonic nanomaterials. These Au nanoparticle clusters also exhibit high photothermal stability during circulation tests. Finally, we discuss the cancer treatment performance of the optimized Au nanoparticle clusters and prove their high PTT performance *in vitro* and *in vivo*.

RESULTS AND DISCUSSION

Theoretical Analysis of PNCs. In principle, the optical response of a nanoparticle cluster system can be described by the multilayer model, as depicted in Figure 1a. 30,31 In this model, the light beam with power I_0 impinges from the topside onto the multilayer system, with each layer consisting of randomly distributed Au nanospheres, where the backward and forward optical powers across the nth and nth layers ($I_{\text{back},n}$, $I_{\text{forw},n}$, $I_{\text{back},n+1}$, and $I_{\text{forw},n+1}$) can be related by the following matrix:

$$\begin{bmatrix} I_{\text{back},n+1} \\ I_{\text{forw},n+1} \end{bmatrix} = \begin{bmatrix} \frac{1}{t_n} & -\frac{r_n}{t_n} \\ \frac{r_n}{t_n} & \frac{t_n^2 - r_n^2}{t_n} \end{bmatrix} \begin{bmatrix} I_{\text{back},n} \\ I_{\text{forw},n} \end{bmatrix}$$
(3)

where t_n and r_n are the transmission and reflection coefficients at the nth layer. Although the above matrix explicitly reflects

the optical response of the PNC, it is difficult to determine the relevant parameters, such as t_n , r_n and the layer number for a specific case. Here, we treat the PNC as an effective medium to avoid potentially tedious calculations, as shown in the middle panel of Figure 1a.32 In the EMA framework, spherical metal inclusions are embedded in a dielectric matrix to form an electromagnetically homogeneous composite. The local field in this composite material can be obtained by the sum of the dielectric response of the matrix and the additional field induced by the surface charge of the metal inclusions. Although the EMA theory does not account for the dipoledipole interactions inside the medium, it can accurately predict the resonance profile of an effective medium made of microand nanostructures, showing good agreement with the results obtained by the time-consuming discrete dipole approximation (DDA) method.³³ In our case, the EMA theory is implemented by dividing the volume of the medium (e.g., water) by the number of plasmonic nanoparticles (e.g., Au) inside our PNC system (inset in Figure 1b). Using the Maxwell-Garnett approximation, we find that the resonant wavelength for a $130 \times 26 \times 26$ nm³ nanoellipsoid made of the Au-water effective medium red shifts from 540 to 964 nm when the filling factor (FF) of Au increases from 0.3 to 1 (Figure 1b and Figures S2 and S3). Although the Maxwell-Garnett approximation is not accurate for FF larger than $\pi/6$ (or 0.4), 34,35 the red shift of the PNC resonance wavelength still holds as it results from the effective permittivity transitioning from water to gold with increasing the PNC FF.

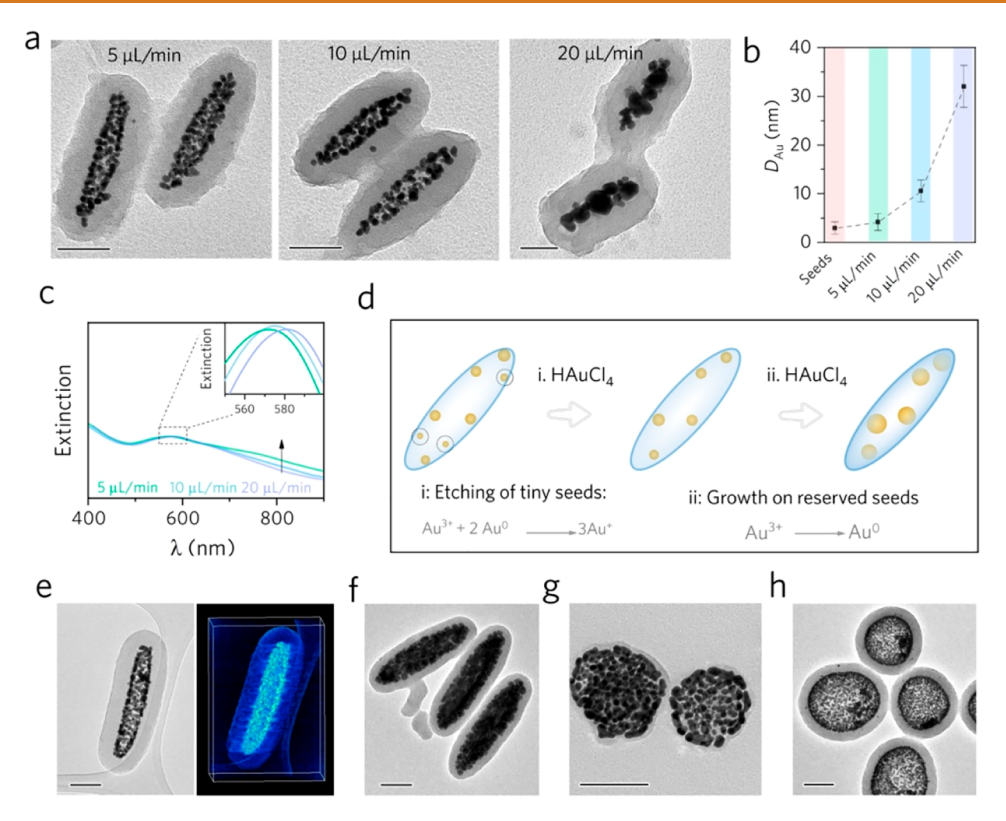


Figure 3. Controlled space-confined seeded growth. (a) TEM micrographs of Au-based PNCs prepared by adding HAuCl₄ at injection rate varying from 5 to $10\,\mu\text{L/min}$ and $20\,\mu\text{L/min}$. Scale bars are all 50 nm. (b) Average sizes of Au nanoparticles within the RF nanocapsules for the three samples in (a), along with the average size of seed nanoparticles. The data were collected by randomly measuring 50 Au nanoparticles for each sample. (c) UV-vis-NIR spectra of the three samples in (a). (d) Schematic illustration of space-confined seeded growth, including the etching of tiny Au seeds and successive seeded growth on reserved seeds. (e-h) TEM micrographs of rod-like Ag (e) and Cu (f) PNCs, and plate-like (g) and spherical (h) Au PNCs. Scale bars are all 100 nm.

To understand the optical response of PNCs with larger FFs, we take a one-dimensional Au nanoparticle chain embedded in water as a model system to resemble the longitudinal axis of an ellipsoid-like PNC. Note that the long axis contributes to the significant absorption of the PNC in the near-infrared (NIR) domain. In this case, we quantitatively calculate the absorption, scattering, and extinction cross sections of the nanoparticle chain using three-dimensional full-wave electrodynamic simulations, as shown in Figure 1c. When the distance between two neighboring Au nanospheres decreases (corresponding to an increase in the PNC FF), the absorption cross section grows dramatically, while the absorption efficiency remains almost the same (see detailed simulation results and relevant discussion in the Supporting Information, part 3). The maximum absorption efficiency can be above 95% even when the gap distance is only 0.5 nm, in contrast to that of a solid gold nanorod (<70% for the case of FF = 1.0 in Figure 1b). Therefore, the main interest of using PNCs instead of anisotropic structures as PTAs is that they can reduce the scattering effect, which is critical to achieving high absorption efficiency. Here, reducing the gap size brings about two-fold benefits: first, the resonance peak red shifts to a longer wavelength being within the first biowindow, guaranteeing a larger penetration depth in the PTT treatment; second, the boosted collective plasmon coupling among Au nanospheres induces a significant local temperature increase due to the enlarged absorption cross section, leading to a more pronounced PTT effect. Overall, coupling the EMA theory and full-wave electrodynamics simulation can guide the design

of the desired PNC structures by relating their FF to the plasmon resonant frequency and absorption efficiency, equivalently revealing the advantages of more densely packed PNCs.

Synthesis of Au Nanoparticle Clusters. Conventional fabrication methods of PNCs based on nanoparticle assembly by noncovalent interaction result in nanoclusters that are not stable against environmental changes. Although such a shortcoming can be solved by forming stable PNCs through the cross-linking of surface polymers from the adjacent gold nanoparticles, 36,37 the assemblages always suffer from a large size of several hundred nanometers, which is not conducive to blood circulation and cell uptake. Moreover, fabricating nanoclusters with a high FF to endow them with absorption at the biowindow is challenging. To solve such a problem, we here propose a space-confined seeded growth strategy (Figure S5) to produce PNCs with high FFs and small overall sizes, which involves (1) synthesis of FeOOH nanorods, (2) loading Au seeds on FeOOH nanorods (FeOOH/Au), (3) coating FeOOH/Au nanorods with resorcinol formaldehyde (RF), (4) selective etching of inside FeOOH, and (5) growth of Au nanoparticles inside capsules. The advantages of this method mainly include (1) controlling the size and gap of nanoparticles and plasmonic coupling by adjusting the precursor amount, thereby verifying the reliability of EMA theory in the prediction of PNCs' optical properties; (2) achieving a high FF that was not possible previously; and (3) enabling stable plasmonic coupling by encapsulating the nanoparticles inside the nanospace.

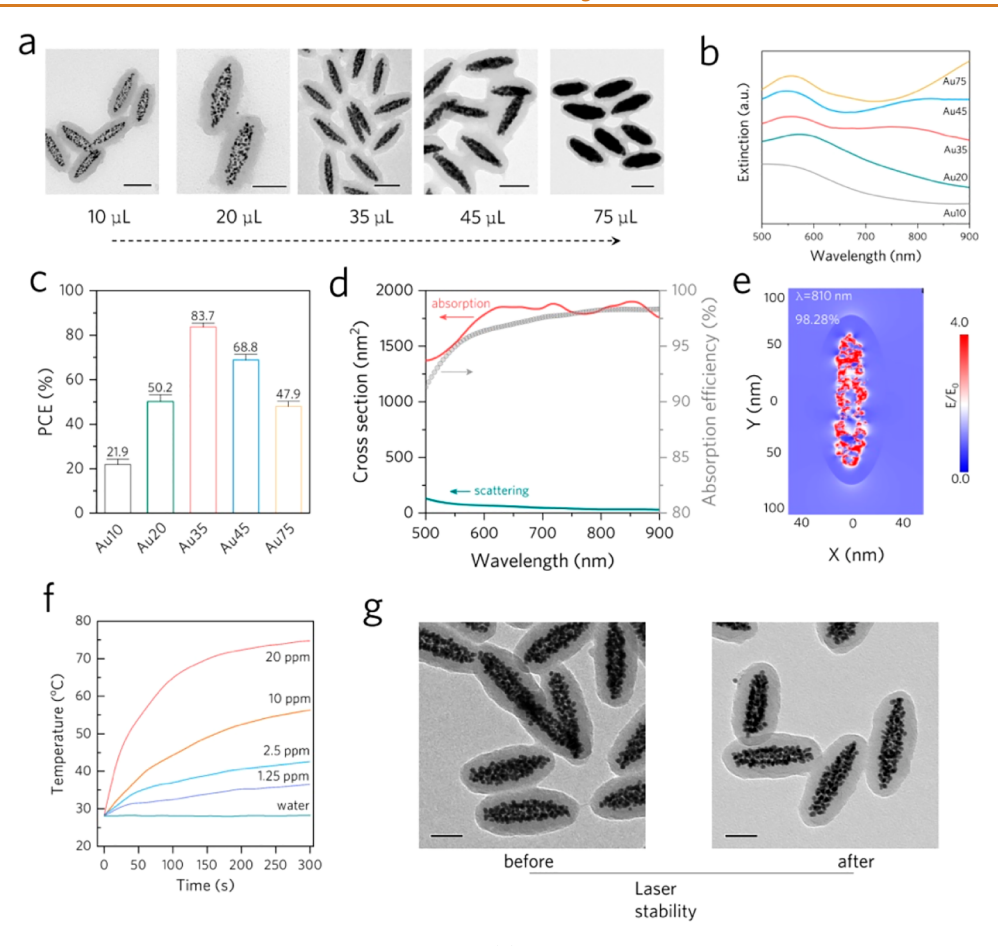


Figure 4. Photothermal conversion capability of Au-based PNCs. (a) TEM micrographs of the Au-based PNCs prepared by injecting different amounts of precursor solution at an injection rate of 5 μ L/min. Scale bars all are 50 nm. (b) UV-vis-NIR spectra of corresponding colloidal dispersions for the samples in (a). (c) Measured photothermal conversion efficiencies for the samples in (a). (d) Simulated absorption and scattering cross sections and calculated absorption efficiency for the Au35 sample. (e) Electric near-field enhancement distribution in the Au35 cluster at 810 nm. (f) Temperature evolution for the Au35 sample of four different concentrations under 808 nm laser irradiation (1.0 W/cm²), along with the result for DI water. (g) TEM micrographs of Au35 before and after laser irradiation for five cycles. Scale bars are both 50 nm.

The uniform ellipsoidal FeOOH nanorods with an average dimension of 125×25 nm were prepared by direct hydrolysis of FeCl₃ in an aqueous solution as initial templates (Figure 2a).³⁸ Subsequently, tetrakis(hydroxymethyl)phosphonium chloride (THPC)-capped tiny Au seeds (size ≤3 nm) were synthesized and then attached to the surface of FeOOH nanorods (FeOOH/Au, Figure S6). An RF layer of 27 nm was then coated on FeOOH/Au nanorods (Figure 2b), and the inside FeOOH nanorod was successively etched away by oxalic acid to create space confinement (Figure 2c). It is emphasized that RF was chosen as the shell material because it not only exhibits relatively good molecular permeability to enable penetration of precursors³³ but also acts as a reducing agent to HAuCl₄ (Figure S7).³⁹ When we directly mixed nanocapsules (Figure 2c) with HAuCl₄ at room temperature, the color of the reaction solution changed gradually from brown to red to dark blue, indicating the formation of Au nanoparticle clusters (Figure 2d). The high-angle annular dark-field scanning transmission electron microscopy (HADDF-STEM) and elemental mapping analyses (Figure S8) reveal the distribution of Au in the core rather than the shell, confirming the high permeability of the RF shells, which enables the exclusive growth of Au on the encapsulated seeds.

Electron Tomography of Au Nanoparticle Clusters.

The detailed structure of Au nanoparticle clusters was analyzed with the help of electron tomography by rotating the sample on a TEM grid at a specific tilt series from -70° to $+70^{\circ}$ with 2° intervals. No noticeable mass loss or radiation damage was observed during the data acquisition process. TEM images at typical rotation angles $(-60, -30, 0, +30, \text{ and } +60^{\circ})$ are shown in Figure 2d. One of the typical 3D-reconstructed Au nanoparticle clusters with different viewing angles is given in Figure 2e $(0, 90, 180, \text{ and } 270^{\circ}, \text{ Figure S9}$ and Movie S1), proving the random distribution of Au nanoparticles inside the RF nanocapsules. The continuously porous nanostructure was further confirmed by electron tomography ortho-slices (Figure 2f) from the x-z plane (Figure 2g, Figure S10, and Movie S2) and x-y plane (Figure 2h and Movie S3).

Mechanism of Space-Confined Seeded Growth. Further investigation reveals that the morphology and optical properties of the products are greatly impacted by the reaction kinetics, which can be controlled by the injection rate of HAuCl₄. When the Au precursor was injected quickly at 20 μ L/min into the reaction system, only a few large Au nanoparticles with an average diameter of 31.2 nm were observed (Figure 3a,b). On the contrary, we obtained many small Au nanoparticles (4.4 nm) inside the RF capsules with a

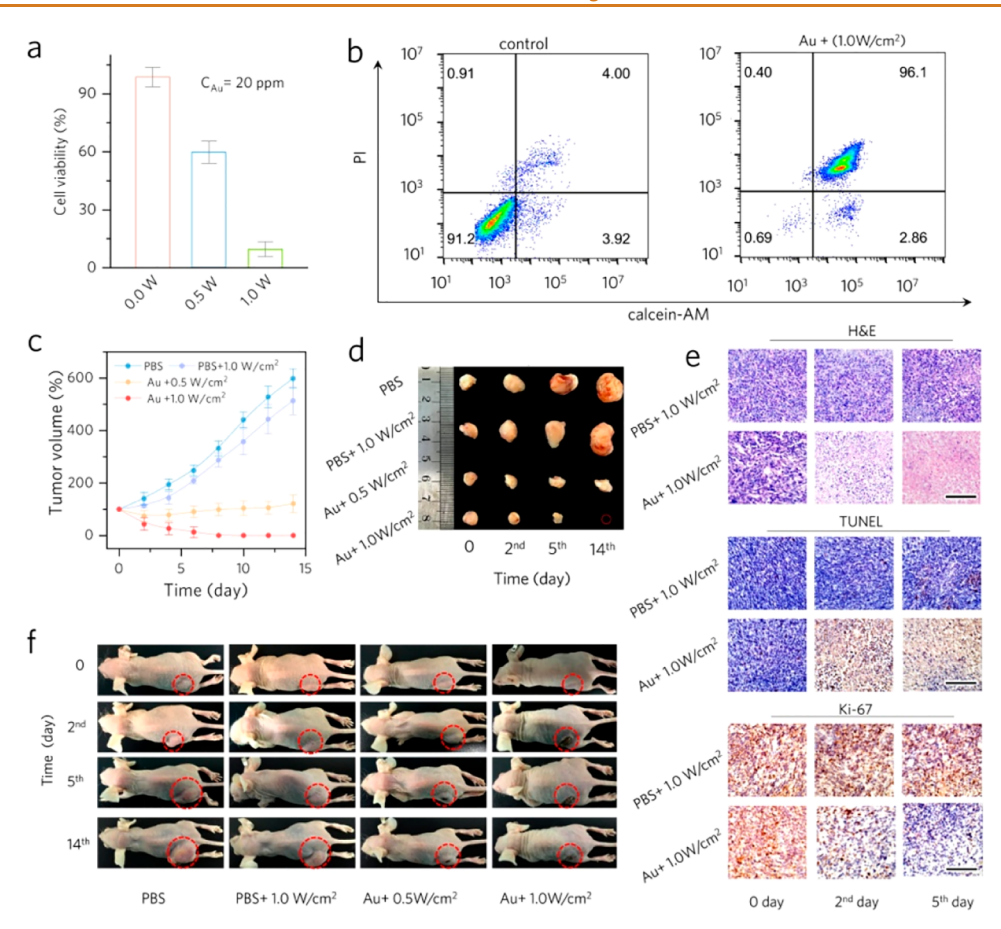


Figure 5. In vivo photothermal therapy. (a) Relative viabilities of 4T1 cells after co-incubation with the Au35 dispersion (20 ppm) under 808 nm laser irradiation at different power densities. (b) Viability of 4T1 cells incubated in PBS and Au35 solution (20 ppm) for 24 h and then irradiated with an 808 nm laser for 5 min (1.0 W/cm²). (c) Relative tumor volume under different treatments. (d) Photographs of tumors extracted from the mice after corresponding treatments in (c). (e) Histological H&E, TUNEL, and Ki-67 staining images of excised tumors of different groups. Scale bars are all 100 μ m. (f) Representative photographs of four groups of 4T1-tumor-bearing mice after various treatments during 14 days.

lower injection rate of 5 μ L/min. Such a difference results from the competition between the dissolution and growth of seeds, with the former being driven by the oxidation of Au⁰ by Au³⁺ ions (Figures 3d and S11) and the latter the reduction of Au³⁺ by the RF shell.⁴⁰ In this experiment, the reduction rate of Au³⁺ is limited by the RF shell. Therefore, a slow injection rate of Au3+ ions ensures that all of the Au seeds had an equal chance to grow. When the injection rate of the Au source increases, the excess number of Au3+ reacts with Au0, resulting in a reduced number of the Au nanoparticles and an increase in the particle sizes. We confirmed this hypothesis by adding sodium oleate as capping ligands to protect the seeds against oxidation because the capping ligands can bind with Au³⁺ ions to lower their reduction potential. As shown in Figure S12, the morphology of small nanoparticles was well-maintained. Consistently, we observed an increasing plasmonic coupling resonance at ~750 nm with reduction of the injection rates (Figure 3c).

We further demonstrated that space-confined seeded growth is a universal strategy. By changing the shape of the template and the type of metal precursors, the morphology and composition of PNCs can be customized. For example, when the AgNO₃ or CuCl₂ was used as a precursor, the rod-shaped Ag (Figure 3e) or Cu (Figure 3f) nanoparticle clusters were produced. By replacing the rod-shaped templates with

nanoplates or nanospheres, we can prepare other anisotropic PNCs (Figure 3g,h). We propose a simple strategy to check the anisotropic morphology of the product by comparing the size of the product and the initial template. When the size of the product is the same as the original template, the growth of the product should strictly follow the templates. Here, the size of the initial nickel hydroxide (\sim 107 nm) and the size of the subsequent growth of Au (\sim 112 nm) are perfectly matched, indicating that the RF capsule has not significantly deformed during the growth, thus inferring the plate-like structure of the products. Similarly, we confirm that the products in Figure 3h are spherical.

Photothermal Effect of Au Nanoparticle Clusters. Another advantage of the space-confined seeded growth method is that we can continuously and accurately tune the optical properties of PNCs because the size of Au nanoparticles and consequently the interparticle distance can be controlled by adjusting the amount of the Au precursors. As shown in Figure 4a,b, with the addition of 10 μ L of Au precursor, the sizes of the seeds (~8.4 nm) have not changed much, leaving large gaps between them. The sample shows a unimodal spectrum around 532 nm. Continuous injection of the Au precursor leads to an increase in the particle sizes and a red shift of the plasmonic peak to 576 nm. A coupling peak at ~780 nm starts to emerge when 35 μ L of HAuCl₄ is injected.

Further increase in the Au precursor causes the small Au nanoparticles to join together, which reduces the plasmonic coupling. The particles finally form nonporous Au nanorods with an average dimension of 60×175 nm.

The photothermal conversion of the above five samples was carefully tested by illuminating the Au nanoparticle solutions (normalized to the same atomic Au concentration) with a NIR laser (Figure S13). The temperature of all samples increased significantly within 5 min and reached the plateau, while the Au35 showed the highest heating rates and equilibrium temperature (Figure S14). To further understand the contribution of plasmon coupling to heat generation, the PCE of all five samples was calculated (see details in the Supporting Information, part 7-III). As shown in Figure 4c, Au35 has the highest PCE of 84%, much higher than that of the other Au nanostructures reported in the literature (Figure S15). The high PCE of Au35 was then analyzed by finitedifference time domain (FDTD) simulations with the help of the electron tomography-assisted true 3D reconstruction process. The σ_{abs} and σ_{scs} of Au35 were calculated and validated by approximating spheres with a slight deviation (Figure S16). As shown in Figure 4d, the absorption cross section reaches the maximum in the wavelength range from 630 to 850 nm. The broadening of the absorption peak can be ascribed to the probable multiple or high-order scattering effects, which are triggered by the multiple built-in hotspots inside the cluster. 29,41-44 We focus on the absorption efficiency at around 810 nm as the wavelength of the laser used here is 808 nm. Our nanostructure has an extremely high absorption efficiency of 98.28% at 810 nm. By plotting the electric field at 810 nm (Figure 4e), we found a substantial electric field enhancement, which should be attributed to the high absorption ability that can be qualitatively evaluated by eq 1 in the Supporting Information, part 3.

We then investigated the relationship between the photothermal properties and the concentrations of Au35 (0, 1.25, 5, 10, and 20 ppm) under an 808 nm laser irradiation (1.0 W/cm²). As expected, upon laser irradiation, the Au35 showed a concentration-dependent temperature increase (Figure 4f). A similar trend is also found with a lower power density irradiation (Figure S17). Laser on—off circulation tests showed no observable change in the overall morphology and average particles size (9.62 \pm 0.4 nm without irradiation vs 9.79 \pm 0.6 nm with irradiation) of the Au35 after five heating cycles (Figures 4g and S18), thus demonstrating the high photothermal stability of Au35. 10

In Vitro Photothermal Therapy. We first evaluated biocompatibility, an important factor for the application of inorganic nanomaterials in biosystems, through in vitro cell cytotoxicity assay of Au35 on human breast cancer cells (MCF-7), mouse breast cancer cells (4T1), and human cervical cancer cells (HeLa) using cell counting kit-8 (CCK-8). The results showed that all of the cells were of nearly identical cell viability (above 90%) with the control group after coincubation with Au35 with a concentration as high as 50 ppm for 24 h (Figure S19), indicating good compatibility of Au35 nanoparticles (Figure S20).

The potential of Au35 for efficient PTT of cancer was evaluated *in vitro* on 4T1 cells. The results showed that Au35 could lead to cell death in a laser-power-dependent manner (Figure 5a). When the cells were incubated with 20 ppm Au35 and then irradiated with an 808 nm laser of 1.0 W/cm², over 90% of them died. The superb photothermal killing efficiency

of the synthesized nanomaterials was further evaluated visually using a confocal laser scanning microscope (Figure S21) and quantitatively based on a flow cytometer (Figure 5b and Figure S22). All cells were stained with calcein-AM for better visual differentiation, which causes green fluorescence in the live cells, and propidium iodide (PI) that characterizes the dead cells with red fluorescence. Consistent with the results of CCK-8, more dead cells can be seen with the increasing nanoparticle concentration and laser power. Almost all cells, including control cells and the cells co-incubated with different concentrations of Au35, were alive when the light irradiation was absent. However, few alive cells can be found within any field of view when the cells were cocultured with gold nanomaterials of 20 ppm and irradiated with an 808 nm laser of 1.0 W/cm². Accordingly, the results from the flow cytometer showed that only 0.69% of the treated cells were alive (cocultured with Au35 of 20 ppm and irradiated with 808 nm laser of 1.0 W/cm²), which is much lower than that of control cells (91.2%). These results from CCK-8, confocal laser scanning microscopy, and flow cytometry suggest the high PTT efficiency of Au35.

In Vivo Photothermal Therapy. Under the permission of the Animal Welfare and Ethics Committee of the Army Medical University, the tumor model was established by injecting 4T1 cells subcutaneously on female BALB/c nude mice. The mice bearing xenografted 4T1 tumors were administered Au35 and then irradiated under the same laser to evaluate the PTT efficiency in vivo. We explored the deep tissue photothermal activity using chicken breast as a model tissue to emulate the clinical scenario. For example, when 10 mm of the tissue was placed between the PNC dispersion (20 μ g/mL) and a laser source (1.0 W/cm²), efficient heating of the aqueous dispersion was achieved (15 °C) without a significant temperature increase inside the tissue (Figure S23). When the tumor volume reached 100 mm³, the tumor-bearing mice were randomly assigned to four groups (five mice per group): phosphate-buffered saline (PBS) group (G1), PBS + laser (1.0 W/cm²) group (G2), Au + laser (0.5 W/cm²) group (G3), and Au + laser (1.0 W/cm^2) group (G4). The Au35 was injected into G3 and G4 percutaneously at a dose of 20 ppm, while an equal volume of PBS was injected into G1 and G2. All lesions were then irradiated with an 808 nm laser for 5 min, with the local temperature being recorded in real-time by a thermal camera. Compared with G2, the local temperatures of G3 and G4 were significantly increased under irradiation of the laser. The laser with a higher power of 1 W/cm² resulted in a temperature increase ($\Delta T = 22.97 \pm 2.51$ °C) much higher than the one of 0.5 W/cm² ($\Delta T = 11.42 \pm 0.12$ °C) within 5 min (Figure S24). These results reveal the satisfactory PCE of the Au35 for PTT in vivo.

Figures 5c and S25 show the relative tumor volume of each group. After treatment, the tumor volume of G1 and G2 increased gradually with a similar growth rate. On the 14th day, the tumor volume was 5.3 and 4.3 times larger than that before the treatment in G1 and G2, respectively. The tumor growth in G3 was suppressed, showing only a slight increase in the tumor volume on the 14th day. On the contrary, the tumor dwindled gradually and eventually disappeared on the 14th day in G4, indicating the superb PTT performance. Representative photos of mice and the resected tumor before and after treatment in different groups are shown in Figure 5d, confirming the quantitative results visually.

The tumors were further excised, fixed, and sliced for histopathological and immunohistochemical analysis using hematoxylin and eosin (H&E) staining and TUNEL assays (Figure 5e). Compared with G2, obvious cell apoptosis and necrosis were observed in the tumor of G4. On the fifth day, few alive cells with intact structures were found in G4. Visualized results are also obtained for the nuclear antigen Ki-67, positively correlated with cell proliferation. Different from the control group, which presents strong Ki-67 expression, almost no Ki-67 can be found in the Au + 1.0 W/cm² group. These results indicated that the efficient photothermal ablation of tumor-mediated Au nanoparticle clusters was achieved by inducing cell necrosis and suppressing cell proliferation.

In addition to the biocompatibility assay in vitro, the biosafety of the nanoparticles was also evaluated in vivo. The body weights of all of the mice were measured, and negligible fluctuations were observed (Figures 5f and S26). After being sacrificed, the main organs, including the heart, liver, spleen, lung, and kidney, were fixed and sliced for H&E staining. There were no obvious morphology changes and cell necrosis found in G4 compared with the control group (Figure S27). We further tested the blood routine and biochemistry after injection of nanoparticles to evaluate the biosafety, including 20 parameters: the urea, creatinine (CREA), uric acid (UA), alanine aminotransferase (ALT), aspartate aminotransferase (AST), alkaline phosphatase (ALP), total protein (TP), total bilirubin (TBIL), white blood cells (WBC), hemoglobin (HGB), red blood cells (RBC), platelet (PLT), hematocrit (HCT), mean corpuscular volume (MCV), mean corpuscular hemoglobin (MCH), mean corpuscular hemoglobin concentration (MCHC), red blood cell distribution width-standard deviation (RDW-SD), red blood cell distribution widthvariation coefficient (RDW-CV), mean platelet volume (MPV), and platelet distribution width (PDW) (Figure S28). The blood biochemistry results show that the renal function markers, including UREA, CREA, and UA values, are constant in the normal range after nanoparticle injection, indicating that the kidney has good function. The other five indicators, including ALT, AST, ALP, TP, and TBIL, which are the main indices of liver function, also are constant in the normal range. After nanoparticle injection at the dosages of 5 and 7.5 mg/kg, there is no obvious increase of ALT, AST, ALP, and TBIL values and no obvious decline of TP, suggesting the good function of the liver. The hematological evaluation was determined by the other 12 parameters. The results show no statistical difference of all the hematological parameters in the treated groups (5 and 7.5 mg/kg) from the control group at all time points. So, we conclude that the nanoparticles synthesized in the present study show trivial side effects and systemic toxicity of Au35 on the health of mice.

CONCLUSIONS

In summary, Au nanoparticle clusters with an ultrahigh PCE of \sim 84% for efficient PTT were prepared by a scalable space-confined seeded growth method. The controlled growth enables the formation of the rod-shaped assemblages of Au nanoparticles with well-distributed gaps, which results in strong plasmonic coupling, significant absorption in the NIR spectrum, and ultimately excellent efficiency in photothermal conversion. Furthermore, the high efficacy of the Au nanoparticle clusters in photothermal ablation of tumors has been fully demonstrated in the *in vitro* and *in vivo* studies,

giving these tailor-designed biocompatible nanostructures a great potential for clinical translation.

METHODS

Synthesis of FeOOH Nanorods. A 400 mL solution containing 0.1 M FeCl $_3$ ·6H $_2$ O in deionized (DI) water was transferred to a 500 mL glass bottle and then heated at 40 °C in an oven for 30 h. The solution was cooled to room temperature and stored at 4 °C before use.

Synthesis of THPC-Capped Gold Seeds. Briefly, 96 mL of water, 0.315 mL of 2.0 M NaOH, 0.126 mL of 16 wt % THPC aqueous solution were mixed in an Erlenmeyer flask for 5 min at which time 0.42 mL of 0.254 M HAuCl₄ was quickly added. The color of the mixture underwent a sudden change from colorless to dark brown. The as-synthesized gold seeds were further aged at 4 $^{\circ}$ C for approximately 2 weeks before use.

Synthesis of FeOOH/Au Nanorods. The as-synthesized FeOOH dispersion (60 mL) was centrifuged at 15000 rpm for 10 min, and the precipitates were further washed with DI water three times. The nanorods were then modified with polyethylenimine (PEI) by dispersing the nanorod in 1 mL of PEI solution (10 mg/mL) for 4 h. After that, the nanorods were isolated by centrifugation (15000 rpm × 10 min) and washed with DI twice to remove the unbound PEI. The as-obtained PEI-modified FeOOH nanorods were then dispersed in 10 mL of gold seed solution and stored overnight. The FeOOH/Au nanorods were separated by centrifugation (15000 rpm × 5 min) and washed with water twice before use.

Synthesis of FeOOH/Au@RF Nanorods. The surface coating of resorcinol formaldehyde was carried out using the Stöber method. The surface of FeOOH/Au nanorods was modified with poly(acrylic acid) (PAA) prior to RF coating. The FeOOH/Au nanorod dispersion was dropwise added into 10 mL of PAA ($M_{\rm n}=1800,\,10$ mg/mL) solution and kept under stirring for 4 h. The nanoparticles were separated by centrifugation and redispersed in 28 mL of water containing 15 mg of resorcinol, 21 μ L of formaldehyde, and 100 μ L of diluted ammonia (2.8 wt %). The solution was then heated to 50 °C for 2 h and boiled at 100 °C for 4 h. The nanoparticles were isolated by centrifugation and redispersed in 15 mL of water.

Selective Etching of FeOOH. The as-prepared FeOOH/Au@RF nanorods were dispersed in 20 mL of oxalic acid solution (2 mol/L), heated to 60 °C, and maintained for 4 h. The hollow seeds were isolated by centrifugation, washed four times, and redispersed in 15 mL of water (seed solution).

Seeded Growth of Au Nanoparticle Clusters. The seeded growth of Au nanoparticle clusters was performed by directly adding HAuCl₄ into the above seed solution. In detail, 50 μ L of the above seed solution was mixed with 1 mL of water to form a reaction solution. Then the precursor solution (HAuCl₄, 25 mM) was carefully injected into the reaction solution by a syringe pump at an injection rate of 5 μ L/min. The reaction solution was stirred for an additional 30 min, and the products were isolated by centrifugation (125000 rpm \times 2 min) and washed with water twice.

In Vitro Photothermal Conversion Assay. To investigate the relationship between photothermal properties and nanoparticles concentrations, 500 μ L of aqueous Au35 nanoparticle dispersions with different concentrations (0, 1.25, 5, 10, and 20 ppm) was irradiated under an 808 nm laser at a power density of 0.5 or 1.0 W/cm² for 5 min. An infrared camera (FLIR A300, USA) was used to record the temperature every 20 s. Photothermal stability of the Au35 was also analyzed by repeating irradiation on/off cycles five times, in which the 20 ppm Au35 nanoparticle dispersion was irradiated under an 808 nm laser (1.0 W/cm²) for 5 min and then cooled at room temperature for another 5 min for every cycle. The infrared camera was also used to monitor the temperature every 20 s.

In Vitro and In Vivo Biocompatibility Assay. Human breast cancer cells (MCF-7), mouse breast cancer cells (4T1), and human cervical cancer cells (HeLa) were used to evaluate the biocompatibility of Au35 using CCK-8 assay in vitro. 4T1 cells were purchased from Procell Life Science & Technology (Wuhan, China). MCF-7

cells and HeLa cells were purchased from the Cell Bank of Type Culture Collection of the Chinese Academy of Sciences (Shanghai, China). All cells were routinely cultured in complete DMEM (C-DMEM) which consisted of 90% DMEM, 100 U/mL penicillin, 100 μ g/mL streptomycin, 2 mM L-glutamine, and 10% fetal bovine serum at 37 $^{\circ}\text{C}$ in a 5% CO_2 humidified incubator (Thermo, Waltham, MA, USA). For the CCK-8 assay, all of the cells were seeded in 96-well plates at a density of approximately 5×10^3 cells per well and incubated overnight. The cells were then incubated with 100 μ L of fresh C-DMEM containing Au35 of different concentrations (0, 1.25, 2.5, 5, 10, 20, 50, and 100 $\mu g/mL$) for 24 h. The cells were then washed with PBS three times, and further cultured with 100 μ L of fresh C-DMEM containing 10% 2-(2-methoxy-4-nitrophenyl)-3-(4nitrophenyl)-5-(2,4-disulfophenyl)-2H-tetrazolium (WST-8) solution. After a 1.5 h co-incubation, the optical density value was measured at 450 nm using a Varioskan flash microplate spectrophotometer (Thermo, Waltham, MA, USA). The relative cell viability was acquired by calculating the percentage of viable cells in total cells.

Under the permission of the Animal Welfare and Ethics Committee of the Army Medical University, female C57 mice (5 weeks old), purchased from Beijing Huafukang Biotechnology Co., Ltd., were injected intravenously with a Au35 suspension at a dosage of 5 and 7.5 mg/(kg body weight) or PBS to evaluate the *in vivo* biosafety. After 24 h, mice were sacrificed, and their main organs, including heart, liver, spleen, lung, and kidney, were fixed and sliced for H&E staining. All images were obtained with an optical microscope (DP80, Olympus, Japan). In addition, 0.8 mL of blood was collected at 0.5, 1, 3, and 7 days (3 mice per time point) after nanoparticle injection for blood routine and biochemistry tests.

In Vitro Photothermal Therapy. The potential of Au35 for efficient PTT of cancer was evaluated in vitro on 4T1 cells using the CCK-8 assay. Typically, cells were seeded in 96-well plates at a density of approximately 5×10^3 cells per well and incubated overnight. Then the cells were incubated with 100 μ L of fresh C-DMEM containing Au35 of different concentrations (0, 1.25, 2.5, 5, 10, and 20 μ g/mL) for 1 h. Following that, the cells were randomly assigned to three groups. Cells in group 1 were further cultured for 24 h without any treatment. Meanwhile, cells in groups 2 and 3 were irradiated under the 808 nm laser at a power density of 0.5 or 1.0 W/cm² for 5 min, respectively, and then were subsequently cultured for 24 h. After that, all of the cells in groups 1, 2, and 3 were analyzed using CCK-8 to determine PTT efficiency following the same procedure used in the previous section.

For a better evaluation of the PTT potential, 4T1 cells treated with Au35 were imaged using a confocal laser scanning microscope and counted on a flow cytometer. Similarly, the 4T1 cells were seeded in 96-well plates and then incubated with 100 μ L of fresh C-DMEM containing Au35 of different concentrations (0, 1.25, 2.5, 5, 10, and $20 \,\mu \text{g/mL}$) for 1 h. The treated cells were randomly assigned to three groups for confocal laser scanning. Cells in group 1 were further cultured without any treatment, whereas groups 2 and 3 were irritated under the 808 nm laser of 0.5 or 1.0 W/cm² for 5 min, respectively, and then cultured for 24 h. Cells were washed with precooled PBS three times and then stained with calcein-AM and PI for 30 min in the humidified cell incubator. After the PBS wash, all of the cells were imaged on a confocal microscope (CLSM, Leica SP5) with excitation at 488 and 532 nm. The cells were randomly divided into two groups for flow cytometry analysis and then further cultured without any treatment (group 1) or irradiated with the 808 nm laser of 1.0 W/cm² for 5 min (group 2). After 24 h of culture, cells were collected and stained with the PE Annexin V apoptosis detection kit I and then analyzed on a Beckman Coulter MoFlo XDP flow cytometer (Miami, FL, USA).

In Vivo Photothermal Conversion Assay and PTT. Under the permission of the Animal Welfare and Ethics Committee of the Army Medical University, the human breast cancer model was established by injecting 4T1 cells subcutaneously on the female BALB/c nude mice (4–5 weeks old, ~15 g, purchased from Beijing Huafukang Biotechnology Co., Ltd.). After collection, 1×10^7 4T1 cells were resuspended in 80 μ L of Matrigel (Corning, NY, USA) and injected

on the back of each mouse. When the tumor volume reached 100 mm³, the tumor-bearing mice were randomly assigned to four groups (5 mice per group): PBS group (G1), PBS + laser (1.0 W/cm²) group (G2), Au35 + laser (0.5 W/cm²) group (G3), and Au35 + laser (1.0 W/cm²) group (G4). All of the mice of G3 and G4 were injected the Au35 into tumors percutaneously at a dose of 20 ppm, and an equal volume of PBS was injected for all mice in G1 and G2. All of the lesions were then irradiated with an 808 nm laser for 5 min, and the local temperatures were recorded in real-time by an infrared camera (FLIR A300, USA). In the following 14 days, the body weight and tumor volume of each treated mouse were recorded every other day, and the relative tumor volume was calculated by V/V_0 (V_0 is the initiated tumor volume before laser irritation, whereas V is the tumor volume during the treatment).

Histological and Immunohistochemical Analysis. We performed the histological and immunohistochemical analysis to better understand PTT for the tumor *in vivo*. The tumor tissues were harvested before and 2 and 5 days after irradiation from different groups and fixed in 4% paraformaldehyde and embedded in paraffin. After being sectioned into 4 μ m slices, the tissues were dewaxed, rehydrated, and stained with H&E, TUNEL, and a Ki-67 kit. All images were obtained with an optical microscope (DP80, Olympus, Japan).

Characterization. The sample morphology was characterized by a Tecnai 12 transmission electron microscope. A 200 keV field-emission S/TEM (FEI-Talos) was performed for TEM characterization. The tilt series images were recorded from -70° to $+70^{\circ}$. During the data acquisition process, no noticeable mass loss or radiation damage was observed. The 3D tomograms were reconstructed using a Matlab script package (e-Tomo) written by Robert Hovden (Muller group, Cornell) with contributions from Dr. Huolin L. Xin. UV—vis spectra were measured with an Ocean Optics HR2000 CG-UV-NIR spectrometer. UV—vis—NIR spectra were measured with a Cary 500 UV—vis—NIR spectrophotometer.

ASSOCIATED CONTENT

Supporting Information

The Supporting Information is available free of charge at https://pubs.acs.org/doi/10.1021/acsnano.1c08485.

Effective medium approximation, FDTD simulations, morphological characterizations, photothermal conversion efficiency, *in vitro* therapy, *in vivo* therapy (PDF) Movie S1: The typical 3D-reconstructed Au nanoparticle cluster with different rotation angles (AVI)

Movie S2: The electron tomography of an Au nanoparticle cluster by ortho-slices from the x-z plane (AVI) Movie S3: The electron tomography of an Au nanoparticle cluster by ortho-slices from the x-y plane (AVI)

AUTHOR INFORMATION

Corresponding Authors

Yadong Yin — Department of Chemistry, University of California, Riverside, California 92521, United States;
ocid.org/0000-0003-0218-3042; Email: yadong.yin@ucr.edu

Dangyuan Lei — Department of Materials Science and Engineering, The City University of Hong Kong, Hong Kong 999077, P.R. China; ⊚ orcid.org/0000-0002-8963-0193; Email: dangylei@cityu.edu.hk

Authors

Jinxing Chen — Institute of Functional Nano & Soft Materials (FUNSOM), Jiangsu Key Laboratory for Carbon-Based Functional Materials & Devices, Joint International Research Laboratory of Carbon-Based Functional Materials and Devices, Soochow University, Suzhou, Jiangsu 215123, P.R.

ACS Nano www.acsnano.org Article

- China; Department of Chemistry, University of California, Riverside, California 92521, United States; orcid.org/0000-0001-9254-7430
- Mingfu Gong Department of Radiology, Xinqiao Hospital, Army Medical University, Chongqing 400037, P.R. China
- Yulong Fan Department of Materials Science and Engineering, The City University of Hong Kong, Hong Kong 999077, P.R. China; ⊚ orcid.org/0000-0001-8610-2072
- Ji Feng Department of Chemistry, University of California, Riverside, California 92521, United States
- Lili Han Department of Physics & Astronomy, University of California, Irvine, California 92697, United States
- **Huolin L. Xin** Department of Physics & Astronomy, University of California, Irvine, California 92697, United States
- Muhan Cao Institute of Functional Nano & Soft Materials (FUNSOM), Jiangsu Key Laboratory for Carbon-Based Functional Materials & Devices, Joint International Research Laboratory of Carbon-Based Functional Materials and Devices, Soochow University, Suzhou, Jiangsu 215123, P.R. China; orcid.org/0000-0002-7988-7219
- Qiao Zhang Institute of Functional Nano & Soft Materials (FUNSOM), Jiangsu Key Laboratory for Carbon-Based Functional Materials & Devices, Joint International Research Laboratory of Carbon-Based Functional Materials and Devices, Soochow University, Suzhou, Jiangsu 215123, P.R. China; orcid.org/0000-0001-9682-3295
- Dong Zhang Department of Radiology, Xinqiao Hospital, Army Medical University, Chongqing 400037, P.R. China; orcid.org/0000-0003-0332-1195

Complete contact information is available at: https://pubs.acs.org/10.1021/acsnano.1c08485

Author Contributions

J.C., M.G., and Y.F. contributed equally. J.C. and Y.Y. conceived and designed the experiments. J.C. synthesized materials. M.G. and D.Z. conducted biological experiments. Y.F. and D.Y.L. performed theoretical analysis. L.H., H.L.X., J.F., M.C., and Q.Z. contributed to the characterization of samples. The manuscript was written through the contributions of all authors.

Notes

The authors declare no competing financial interest.

ACKNOWLEDGMENTS

This work was supported in part by the Engineering Research Centers Program of the U.S. National Science Foundation under NSF Cooperative Agreement No. 1941543. J.C. acknowledges the support by the National Natural Science Foundation of China (51901147). L.H. was supported by the startup funding of H.L.X. Q.Z. thanks the support by the National Natural Science Foundation of China (51922073) and the Natural Science Foundation of Jiangsu Province (BK20180097). J.C., M.C., and Q.Z. acknowledge the financial support from the Suzhou Key Laboratory of Functional Nano & Soft Materials, Collaborative Innovation Center of Suzhou Nano Science & Technology, and the 111 Project. D.Y.L. acknowledges the financial support by the National Natural Science Foundation of China through the Excellent Young Scientist Fund (62022001).

REFERENCES

- (1) Yingchoncharoen, P.; Kalinowski, D. S.; Richardson, D. R. Lipid-Based Drug Delivery Systems in Cancer Therapy: What Is Available and What Is Yet to Come. *Pharmacol. Rev.* **2016**, *68* (3), 701–787.
- (2) Sung, H.; Ferlay, J.; Siegel, R.; Laversanne, M.; Soerjomataram, I.; Jemal, A.; Bray, F. Global Cancer Statistics 2020: GLOBOCAN Estimates of Incidence and Mortality Worldwide for 36 Cancers in 185 Countries. *CA: A Cancer J. Clin.* **2021**, *71*, 209–249.
- (3) Chen, Z. Z.; Huang, L.; Wu, Y. H.; Zhai, W. J.; Zhu, P. P.; Gao, Y. F. LncSox4 Promotes the Self-Renewal of Liver Tumor-Initiating Cells through Stat3-Mediated Sox4 Expression. *Nat. Commun.* **2016**, 7, 12598.
- (4) Sarmento-Ribeiro, A. B.; Scorilas, A.; Goncalves, A. C.; Efferth, T.; Trougakos, I. P. The Emergence of Drug Resistance to Targeted Cancer Therapies: Clinical Evidence. *Drug Resist. Update* **2019**, *47*, 100646.
- (5) Liu, Y.; Bhattarai, P.; Dai, Z.; Chen, X. Photothermal Therapy and Photoacoustic Imaging *via* Anotheranostics in Fighting Cancer. *Chem. Soc. Rev.* **2019**, *48*, 2053–2108.
- (6) Hu, K.; Xie, L.; Zhang, Y.; Hanyu, M.; Yang, Z.; Nagatsu, K.; Suzuki, H.; Ouyang, J.; Ji, X.; Wei, J.; Xu, H.; Farokhzad, O. C.; Liang, S. H.; Wang, L.; Tao, W.; Zhang, M. R. Marriage of Black Phosphorus and Cu²⁺ as Effective Photothermal Agents for PET-Guided Combination Cancer Therapy. *Nat. Commun.* **2020**, *11*, 2778.
- (7) Chu, K. F.; Dupuy, D. E. Thermal Ablation of Tumours: Biological Mechanisms and Advances in Therapy. *Nat. Rev. Cancer* **2014**, *14*, 199–208.
- (8) Li, X.; Lovell, J. F.; Yoon, J.; Chen, X. Clinical Development and Potential of Photothermal and Photodynamic Therapies for Cancer. *Nat. Rev. Clin. Oncol.* **2020**, *17*, 657–674.
- (9) Jaque, D.; Martinez Maestro, L.; Del Rosal, B.; Haro-Gonzalez, P.; Benayas, A.; Plaza, J. L.; Martin Rodriguez, E.; Garcia Sole, J. Nanoparticles for Photothermal Therapies. *Nanoscale* **2014**, *6*, 9494–530.
- (10) Nam, J.; Son, S.; Ochyl, L. J.; Kuai, R.; Schwendeman, A.; Moon, J. J. Chemo-Photothermal Therapy Combination Elicits Anti-Tumor Immunity against Advanced Metastatic Cancer. *Nat. Commun.* **2018**, *9*, 1074.
- (11) Kim, M.; Lee, J. H.; Nam, J. M. Plasmonic Photothermal Nanoparticles for Biomedical Applications. *Adv. Sci.* **2019**, *6*, 1900471.
- (12) Chen, J.; Bai, Y.; Feng, J.; Yang, F.; Xu, P.; Wang, Z.; Zhang, Q.; Yin, Y. Anisotropic Seeded Growth of Ag Nanoplates Confined in Shape-Deformable Spaces. *Angew. Chem., Int. Ed.* **2021**, *60*, 4117–4124.
- (13) Ali, M. R.; Rahman, M. A.; Wu, Y.; Han, T.; Peng, X.; Mackey, M. A.; Wang, D.; Shin, H. J.; Chen, Z. G.; Xiao, H.; Wu, R.; Tang, Y.; Shin, D. M.; El-Sayed, M. A. Efficacy, Long-Term Toxicity, and Mechanistic Studies of Gold Nanorods Photothermal Therapy of Cancer in Xenograft Mice. *Proc. Natl. Acad. Sci. U S A* **2017**, *114*, E3110—E3118.
- (14) Chen, J.; Ye, Z.; Yang, F.; Yin, Y. Plasmonic Nanostructures for Photothermal Conversion. *Small Sci.* **2021**, *1*, 2000055.
- (15) Gonzalez-Rubio, G.; Diaz-Nunez, P.; Rivera, A.; Prada, A.; Tardajos, G.; Gonzalez-Izquierdo, J.; Banares, L.; Llombart, P.; Macdowell, L. G.; Alcolea Palafox, M.; Liz-Marzan, L. M.; Pena-Rodriguez, O.; Guerrero-Martinez, A. Femtosecond Laser Reshaping Yields Gold Nanorods with Ultranarrow Surface Plasmon Resonances. *Science* 2017, 358, 640–644.
- (16) Gonzalez-Rubio, G.; Guerrero-Martinez, A.; Liz-Marzan, L. M. Reshaping, Fragmentation, and Assembly of Gold Nanoparticles Assisted by Pulse Lasers. *Acc. Chem. Res.* **2016**, *49*, 678–686.
- (17) de Aberasturi, D. J.; Serrano-Montes, A. B.; Liz-Marzán, L. M. Modern Applications of Plasmonic Nanoparticles: From Energy to Health. *Adv. Opt. Mater.* **2015**, *3*, 602–617.
- (18) Jain, P. K.; El-Sayed, I. H.; El-Sayed, M. A. Au Nanoparticles Target Cancer. *Nano Today* **2007**, *2*, 18–29.

- (19) Kim, H. S.; Lee, D. Y. Near-Infrared-Responsive Cancer Photothermal and Photodynamic Therapy Using Gold Nanoparticles. *Polymers* **2018**, *10*, 961.
- (20) Sun, H.; Du, J. Plasmonic Vesicles with Tailored Collective Properties. *Nanoscale* **2018**, *10*, 17354–17361.
- (21) Song, J.; Huang, P.; Duan, H.; Chen, X. Plasmonic Vesicles of Amphiphilic Nanocrystals: Optically Active Multifunctional Platform for Cancer Diagnosis and Therapy. *Acc. Chem. Res.* **2015**, *48*, 2506–2515
- (22) Song, J.; Wu, B.; Zhou, Z.; Zhu, G.; Liu, Y.; Yang, Z.; Lin, L.; Yu, G.; Zhang, F.; Zhang, G.; Duan, H.; Stucky, G. D.; Chen, X. Double-Layered Plasmonic-Magnetic Vesicles by Self-Assembly of Janus Amphiphilic Gold-Iron(II,III) Oxide Nanoparticles. *Angew. Chem., Int. Ed.* **2017**, *56*, 8110–8114.
- (23) Zhu, K.; Liu, G.; Zhang, G.; Hu, J.; Liu, S. Engineering Cross-Linkable Plasmonic Vesicles for Synergistic Chemo-Photothermal Therapy Using Orthogonal Light Irradiation. *Macromolecules* **2018**, *51*, 8530–8538.
- (24) Song, J.; Huang, P.; Chen, X. Preparation of Plasmonic Vesicles from Amphiphilic Gold Nanocrystals Grafted with Polymer Brushes. *Nat. Protoc.* **2016**, *11*, 2287–2299.
- (25) Dhiman, M.; Maity, A.; Das, A.; Belgamwar, R.; Chalke, B.; Lee, Y.; Sim, K.; Nam, J. M.; Polshettiwar, V. Plasmonic Colloidosomes of Black Gold for Solar Energy Harvesting and Hotspots Directed Catalysis for CO₂ to Fuel Conversion. *Chem. Sci.* **2019**, *10*, 6594–6603
- (26) Chen, J.; Feng, J.; Li, Z.; Xu, P.; Wang, X.; Yin, W.; Wang, M.; Ge, X.; Yin, Y. Space-Confined Seeded Growth of Black Silver Nanostructures for Solar Steam Generation. *Nano Lett.* **2019**, *19*, 400–407
- (27) Luk'yanchuk, B.; Zheludev, N. I.; Maier, S. A.; Halas, N. J.; Nordlander, P.; Giessen, H.; Chong, C. T. The Fano Resonance in Plasmonic Nanostructures and Metamaterials. *Nat. Mater.* **2010**, *9*, 707–715
- (28) Halas, N. J.; Lal, S.; Chang, W. S.; Link, S.; Nordlander, P. Plasmons in Strongly Coupled Metallic Nanostructures. *Chem. Rev.* **2011**, *111*, 3913–3961.
- (29) Prodan, E.; Radloff, C.; Halas, N. J.; Nordlander, P. A Hybridization Model for the Plasmon Response of Complex Nanostructures. *Science* **2003**, 302, 419–22.
- (30) Micheli, D.; Vricella, A.; Pastore, R.; Marchetti, M. Synthesis and Electromagnetic Characterization of Frequency Selective Radar Absorbing Materials Using Carbon Nanopowders. *Carbon* **2014**, *77*, 756–774.
- (31) Zhong, Y. K.; Lai, Y. C.; Tu, M. H.; Chen, B. R.; Fu, S. M.; Yu, P.; Lin, A. Omnidirectional, Polarization-Independent, Ultra-Broadband Metamaterial Perfect Absorber Using Field-Penetration and Reflected-Wave-Cancellation. *Opt. Express* **2016**, *24*, A832—A845.
- (32) Niklasson, G. A.; Granqvist, C. G.; Hunderi, O. Effective Medium Models for the Optical Properties of Inhomogeneous Materials. *Appl. Opt.* **1981**, *20*, 26–30.
- (33) Markel, V. A. Introduction to the Maxwell Garnett Approximation: Tutorial. *J. Opt. Soc. Am. A* **2016**, *33*, 1244–56.
- (34) Markel, V. A. Maxwell Garnett Approximation (Advanced Topics): Tutorial. J. Opt. Soc. Am. A 2016, 33, 2237–2255.
- (35) Lamb, W.; Wood, D. M.; Ashcroft, N. W. Long-Wavelength Electromagnetic Propagation in Heterogeneous Media. *Phys. Rev. B* 1980, 21, 2248–2266.
- (36) Chen, Y.; Wang, Z.; He, Y.; Yoon, Y. J.; Jung, J.; Zhang, G.; Lin, Z. Light-Enabled Reversible Self-Assembly and Tunable Optical Properties of Stable Hairy Nanoparticles. *Proc. Natl. Acad. Sci. U S A* **2018**, *115*, E1391–E1400.
- (37) Liu, Y.; Wang, J.; Zhang, M.; Li, H.; Lin, Z. Polymer-Ligated Nanocrystals Enabled by Nonlinear Block Copolymer Nanoreactors: Synthesis, Properties, and Applications. *ACS Nano* **2020**, *14*, 12491–12521.
- (38) Chen, J.; Feng, J.; Yang, F.; Aleisa, R.; Zhang, Q.; Yin, Y. Space-Confined Seeded Growth of Cu Nanorods with Strong Surface

- Plasmon Resonance for Photothermal Actuation. *Angew. Chem., Int. Ed.* **2019**, 58, 9275–9281.
- (39) Yang, P.; Xu, Y.; Chen, L.; Wang, X.; Zhang, Q. One-Pot Synthesis of Monodisperse Noble Metal @ Resorcinol-Formaldehyde (M@RF) and M@Carbon Core-Shell Nanostructure and Their Catalytic Applications. *Langmuir* 2015, 31, 11701–8.
- (40) Lee, Y. J.; Schade, N. B.; Sun, L.; Fan, J. A.; Bae, D. R.; Mariscal, M. M.; Lee, G.; Capasso, F.; Sacanna, S.; Manoharan, V. N.; Yi, G. R. Ultrasmooth, Highly Spherical Monocrystalline Gold Particles for Precision Plasmonics. *ACS Nano* **2013**, *7*, 11064–70.
- (41) Yu, H.; Peng, Y.; Yang, Y.; Li, Z.-Y. Plasmon-Enhanced Light—Matter Interactions and Applications. *npj Comput. Mater.* **2019**, *S*, 45.
- (42) Huang, J.; Liu, C.; Zhu, Y.; Masala, S.; Alarousu, E.; Han, Y.; Fratalocchi, A. Harnessing Structural Darkness in the Visible and Infrared Wavelengths for a New Source of Light. *Nat. Nanotechnol.* **2016**, *11*, 60–66.
- (43) Fan, J. A.; Wu, C.; Bao, K.; Bao, J.; Bardhan, R.; Halas, N. J.; Manoharan, V. N.; Nordlander, P.; Shvets, G.; Capasso, F. Self-Assembled Plasmonic Nanoparticle Clusters. *Science* **2010**, 328, 1135–8
- (44) Urban, A. S.; Shen, X.; Wang, Y.; Large, N.; Wang, H.; Knight, M. W.; Nordlander, P.; Chen, H.; Halas, N. J. Three-Dimensional Plasmonic Nanoclusters. *Nano Lett.* **2013**, *13*, 4399–4403.
- (45) Park, S. M.; Aalipour, A.; Vermesh, O.; Yu, J. H.; Gambhir, S. S. Towards Clinically Translatable *in Vivo* Nanodiagnostics. *Nat. Rev. Mater.* **2017**, 2, 17014.

□ Recommended by ACS

Compact Plasmonic Blackbody for Cancer Theranosis in the Near-Infrared II Window

Jiajing Zhou, Hongwei Duan, et al.

FEBRUARY 13, 2018

ACS NANO

READ 🗹

Realizing a Record Photothermal Conversion Efficiency of Spiky Gold Nanoparticles in the Second Near-Infrared Window by Structure-Based Rational Design

Cuixia Bi, Haibing Xia, et al.

MARCH 29, 2018

CHEMISTRY OF MATERIALS

READ 🗹

Optical and Photothermal Properties of Graphene Coated Au-Ag Hollow Nanoshells: A Modeling for Efficient Photothermal Therapy

Mohsen Farokhnezhad and Mahdi Esmaeilzadeh

NOVEMBER 01, 2019

THE JOURNAL OF PHYSICAL CHEMISTRY C

READ **C**

Hybridized Plasmonic Gap Mode of Gold Nanorod on Mirror Nanoantenna for Spectrally Tailored Fluorescence Enhancement

Hiroshi Sugimoto, Minoru Fujii, et al.

JUNE 22, 2018

ACS PHOTONICS

READ 🗹

Get More Suggestions >